A DIRECT ANALYSIS OF LAMELLAR X-RAY DIFFRACTION FROM HYDRATED ORIENTED MULTILAYERS OF FULLY FUNCTIONAL SARCOPLASMIC RETICULUM

L. HERBETTE, J. MARQUARDT, A. SCARPA, AND J. K. BLASIE, *Department of Biochemistry and Biophysics, School of Medicine, University of Pennsylvania, Philadelphia, Pennsylvania 19174 U.S.A.*

ABSTRACT The profile structure of functional sarcoplasmic reticulum (SR) membranes was investigated by X-ray diffraction methods to a resolution of 10 Å. The lamellar diffraction data from hydrated oriented multilayers of SR vesicles showed monotonically increasing widths for higher order lamellar reflections, indicative of simple lattice disorder within the multilayer. A generalized Patterson function analysis, previously developed for treating lamellar diffraction from lattice-disordered multilayers, was used to identify the autocorrelation function of the unit cell electron density profile. Subsequent deconvolution of this autocorrelation function provided the most probable unit cell electron density profile of the SR vesicle membrane pair. The resulting single membrane profile possesses marked asymmetry, suggesting that a major portion of the Ca^{++}-ATPase resides on the exterior of the vesicle. The electron density profile also suggests that the Ca^{++}-dependent ATPase penetrates into the lipid hydrocarbon core of the SR membrane. Under conditions suitable for X-ray analysis, SR vesicles prepared as partially dehydrated oriented multilayers are shown to conserve most of their ATP-induced Ca^{++} uptake functionality, as monitored spectrophotometrically with the Ca^{++} indicator arsenazo III. This has been verified both in resuspensions of SR after centrifugation and slow partial dehydration, and directly in SR multilayers in a partially dehydrated state (20–30% water). Therefore, the profile structure of the SR membrane that we have determined may closely resemble that found in vivo.

INTRODUCTION

The concept that the sarcoplasmic reticulum (SR) is the principal regulator of the contraction-relaxation cycle in muscle has been firmly established. A detailed picture of the active transport process of ATP-induced Ca^{++} uptake by SR that lowers the ionized Ca^{++} concentration of the sarcoplasm below 10^{-7} M is known to cause muscle relaxation, whereas the passive release of Ca^{++} from SR during depolarization leads to contraction (1, 2). The former function has been studied to a great extent in vesicles of fragmented SR membranes, known to accumulate Ca^{++} against a concentration

---

Dr. Scarpa is an Established Investigator of the American Heart Association.

gradient in the presence of ATP (3, 4). This process occurs very rapidly in vesicular dispersions of SR, attaining steady-state accumulations within 60 s.

Owing to its well characterized and simplified function and composition, the SR membrane constitutes an outstanding system for a structure-function study. The primary function of SR is the fast accumulation of Ca^{++} against a concentration gradient related to a Ca^{++} and Mg^{++}-dependent ATPase of mol wt 102,000 (5, 6). The structure is simplified by the fact that it consists of essentially two phospholipids (phosphatidyl choline and phosphatidyl ethanolamine) and a major protein, the Ca^{++}-ATPase that comprises about 60% of the total protein present in heavy SR vesicles (HSR) and approximately 90% in light SR (LSR) (7-9).

X-ray diffraction from multilayers of SR membranes oriented by centrifugation, followed by slow partial dehydration, can provide meridional lamellar diffraction that arises from the membrane's electron density profile. This profile represents a projection of the electron density distribution of the membrane along a direction parallel to the membrane plane onto an axis normal to that plane (10), and is therefore due to the average distribution of membrane molecular components projected onto this profile axis. The nature of the lamellar diffraction critically depends on the degree and kinds of disorder present in the multilayer. Equatorial diffraction occurring at right angles to the lamellar diffraction arises from the packing of the protein and lipid molecules in the membrane plane (11-13). The nature of the equatorial diffraction can provide information as to the physical state of the lipids (frozen vs. melted hydrocarbon chains), as well as the arrangement of the protein (crystalline vs. liquid) in the membrane plane. In addition to this, diffraction may also arise from the internal structural characteristics of the protein itself. Hence, a vast amount of information can in principle be obtained regarding the membrane's molecular organization with X-ray diffraction obtained from hydrated oriented membrane multilayers. Additional support for the validity of the experimental approach is the demonstration that the membrane under question has retained its primary function in such hydrated oriented multilayers and that this structural information can therefore be obtained under conditions of maximal functional activity of SR vesicles.

The X-ray structure of the SR membrane has been investigated previously by several authors. Worthington and Liu (14), using Patterson-function methods of X-ray structure analysis, reported an SR electron density profile of fully hydrated pellets for a range of lamellar repeat distances between 220 and 270 Å. Likewise, Dupont et al. (15), employing swelling methods of structure analysis, reported an electron density profile for the SR membrane from fully hydrated specimens (50% water by weight, lamellar repeat distance of 270 Å) and a "dry" specimen (25% water, lamellar repeat distance of 170 Å).

We have applied the method of X-ray structure analysis developed by Schwarz et al. (16), which properly accounts for the effects of disorder in the multilayer lattice, to determine the electron density profile of the SR membrane to a resolution of about 10 Å. Whereas previous authors have neglected to account for the substantial degree of disorder in the multilayer lattice, the electron density profile that we have derived

for the SR membrane is the most accurate to date, since it is unperturbed by disorder. Furthermore, SR vesicles prepared as partially dehydrated oriented multilayers for X-ray analysis are shown to conserve most of their ATP-induced Ca^{++} uptake functionality. This has been demonstrated both in resuspensions of SR, assayed after centrifugation and partial dehydration, and directly in hydrated oriented multilayers prepared under conditions identical to those necessary for the X-ray diffraction experiments. Therefore the structure of the SR membrane that we have determined may closely resemble that found in the physiologically intact vesicular network surrounding the myofibrils.

METHODS

Isolation and Purification of SR

SR was isolated by homogenization and differential centrifugation of rabbit hind leg and back white muscle by a procedure modified from that of McFarland and Inesi (17). Dissected muscle was homogenized for 15 s in a Waring Blendor (Waring Products Div., Dynamics Corp. of America, New Hartford, Conn.) every 5 min for 1 h. The pH of the homogenization buffer (0.3 M sucrose, 0.01 M histidine) was maintained at 6.8 by additions of 1 M NaOH. The homogenate was centrifuged for 20 min at 11,250 rpm in an SS-34 Sorvall rotor (DuPont Instruments, Sorvall Operations, Newtown, Conn.). The supernatant was collected through cheesecloth to remove floating fat particles and centrifuged for 90 min at 18,500 rpm. Pellets were resuspended in 48 ml of 0.6 M KCl, 0.01 M histidine, pH 7.0, and incubated for 40 min at 4°C. This fraction was centrifuged for 20 min at 11,250 rpm to remove actomyosin contaminants. The supernatant was centrifuged for 90 min at 18,500 rpm, followed by resuspension of these pellets in 0.9 M sucrose, 0.01 M histidine, pH 7.0. This fraction, designated as crude SR, was then quickly frozen in liquid N_2 and stored at −25°C until use.

Further purification of the preparation involved zonal density gradient centrifugation of this crude SR similar to that done by Meissner et al. (18). Approximately 100 mg of this crude fraction was layered on top of a step function gradient (20–45% sucrose by weight), as established by an LKB ultragrad gradient mixer (LKB Instruments, Inc., Rockville, Md.) in a Ti-14 zonal rotor spinning at 2,000 rpm at 4°C. A 15% sucrose overlay was then added and the rotor was spun for 1 h at 43,000 rpm. After deacceleration to 2,000 rpm, the rotor was unloaded through the center by pumping in heavy sucrose (45%) at the periphery. Samples of 5–10 ml were collected during continuous monitoring of the protein absorbance at 280 nm. For each sample, the sucrose concentration was measured with a Bausch and Lomb refractometer at 25°C (Bausch & Lomb, Inc., Rochester, N.Y.).

Fraction I (18–20% sucrose) was discarded. The LSR, designated as fraction II (22–27% sucrose), was isolated separately in several density subfractions. The heavier density fraction (33–37% sucrose) contained HSR and mitochondria as indicated by the presence of high cytochrome a oxidase activity. Each subfraction of fraction II was diluted two- to fourfold with 100 mM KCl, 2 mM Tris maleate, 10 mM $MgCl_2$, pH 6.8 (medium I), and centrifuged at 18,500 rpm for 90 min. The pellets were resuspended and dialyzed overnight in medium I. The final sucrose in all subfractions was less than 1%. Protein concentrations of crude and purified SR were determined by the method of Lowry.

Ca^{++} Uptake by SR

Ca^{++} uptake by SR was measured by a dual wavelength spectrophotometric technique with arsenazo III as a metallochromic indicator. Under defined conditions, changes in ionized Ca^{++}

concentrations in the reaction mixture produce linear increments of Δ absorbance of arsenazo III. Calibration of the absorbance changes were obtained by adding known amounts of $CaCl_2$ or EGTA to the reaction mixture under identical conditions (19). The changes in absorbance of the dye were measured with a time-sharing multichannel spectrophotometer developed at the Johnson Foundation, University of Pennsylvania, at 675–685 nm, the wavelength pair at which ionized Ca^{++} concentration changes can be measured selectively and without inter-
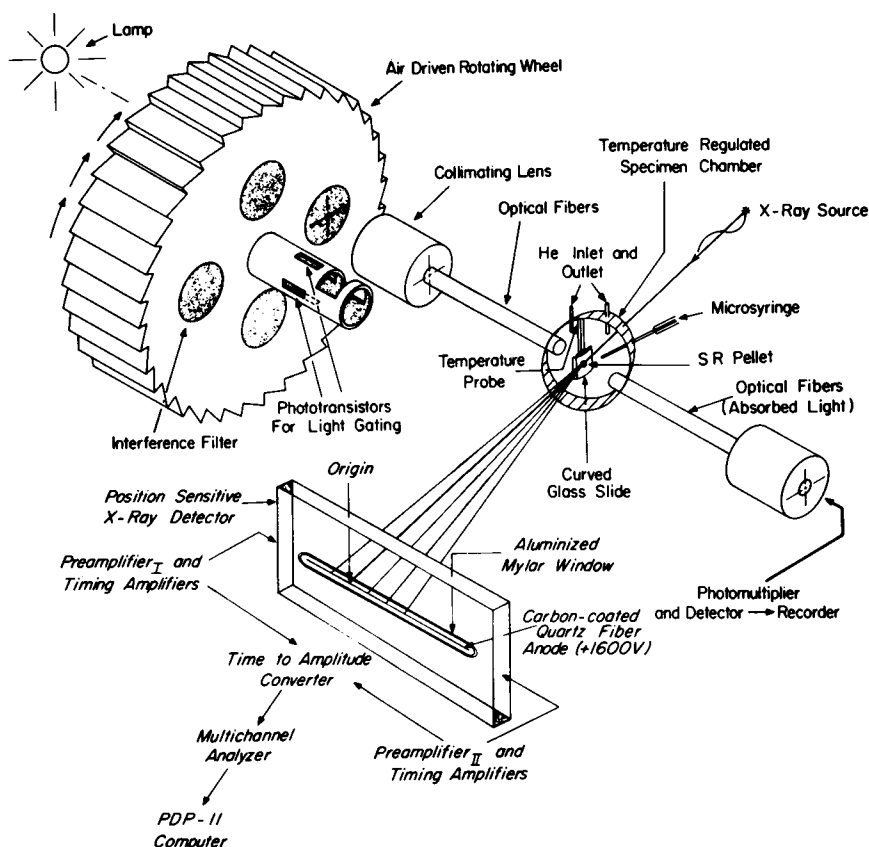
FIGURE 1   Schematic diagram (not to scale) of optical and X-ray diffraction system. The optical system consists of a quartz-iodine lamp, four interference filters (507, 540, 675, and 685 nm) having 40–50% transmittance, and 1 nm half-band width equally spaced in a rotating wheel assembly driven by compressed air at a frequency of 20–5,000 Hz. Light passing through the rotating wheel is collimated and then directed to oriented SR multilayers through flexible light pipes. Similar optic fibers collect the transmitted light passing through SR multilayers, which are then conveyed to the photomultiplier tube. A time-sharing multichannel spectrophotometer detects differences of these four pulses of light with the Δ absorbances displayed on a multi-channel pen recorder. Continuous readout of the changes in absorbance of arsenazo III at 675–685 nm and phenol red at 507–540 nm were possible. Distance between light pipes is about 6 mm, with an average mean path length through the SR multilayers of about 0.5 mm. The incident X-ray beam was positioned perpendicular to the light path and the diffracted X-rays were collected on a position-sensitive X-ray detector. More details of this instrumentation are in the text.

ference from aspecific changes due to volume and/or refractive index changes. ATP-dependent Ca^{++} transport by SR was measured either in dispersions or in hydrated oriented multilayers. The optical arrangement for the multilayer measurements are schematically depicted (not to scale) in Fig. 1. When the dispersion was assayed, a cuvette (1-cm path length) was simply placed between the collimating lens and the photomultiplier and the optical pipes indicated in Fig. 1 were omitted. Experiments involving simultaneous recording of functional activity and X-ray diffraction on oriented SR multilayers at the same temperature and relative humidity are now being carried out in our laboratory and will be reported shortly.

The activity of SR dispersions (1 mg/ml) was monitored in 2 ml final volume of medium I containing 50 μM arsenazo III, pH 6.8, with 50 μM $CaCl_2$. The reaction was started by adding ATP so that its final concentration was 200 μm. In these studies, both crude and purified SR were used.

For the monitoring of activity in SR multilayers, either crude or purified SR (2–3 mg) was resuspended in the same medium containing 200 μm arsenazo III and 115 μm Ca^{++} to a final volume of 2.5 ml. The SR suspension was then centrifuged in a Beckman SW 27 swinging bucket rotor for 3 h at 25,000 rpm on microscope cover slips (Beckman Instruments, Inc., Spinco Div., Palo Alto, Calif.). A special Lucite sedimentation cell with an inner diameter of 1 cm was used, sealed at the bottom by the cover slip (20). These multilayers, either freshly centrifuged or partially dehydrated at 90% relative humidity for 20–24 h at 4°C in sealed glass vials, were then mounted as indicated in Fig. 1. Each specimen was assayed for ATP-dependent Ca^{++} uptake after addition of ATP-Mg to its surface by either atomization or microinjection.

In some control experiments, ATP was added to SR multilayers sedimented in the absence of added Ca^{++} or in the presence of Ca^{++} but with saturating amounts of EGTA. Similar experiments were carried out in which Ca^{++} and EGTA were added directly to the multilayer specimen surface after sedimentation. In a few of these experiments, A23187 or X537A, two ionophores that equilibrate Ca^{++} gradients across SR vesicles (21), were added to the multilayer specimen surface during the steady state after depletion of ATP. Stock solutions of both A23187 and X537A were prepared in ethanol to yield final concentrations of 2 and 3 mg/ml, respectively. A few specimens were centrifuged on aluminum foil in the absence of dyes and either rehomogenized immediately or partially dehydrated at 90% relative humidity and rehomogenized in medium I containing 50 μm arsenazo III and assayed as described above for dispersions. All functional assays were carried out at room temperature.

Formation of Hydrated Oriented Membrane Multilayers

For the X-ray diffraction studies, subfractions of fraction II, purified SR (1 mg), were resuspended in medium I in the absence of any dyes to a final volume of 2.5 ml and centrifuged in a special Lucite sedimentation cell (20) onto aluminum foil strips for 3 h at 25,000 rpm in a Beckman SW 27 swinging bucket rotor. The cell is designed with a lower inner diameter of 5 mm and sealed at the bottom by the aluminum foil strip onto which the sedimented membranes adhere. The aluminum strip was then removed from the sedimentation cell and glued to glass slides 1 cm × 1 cm (length × height) that were a section of a cylindrical shell whose curvature was 0.5 cm^{-1} (see specimen geometry below), and suspended in sealed glass vials over one of several saturated salt solutions whose relative humidities (RH) lie in a range of 81–95% (as measured at 20°C). These specimens were partially dehydrated at a specified RH in this range for 20–24 h at 4°C before exposure.

After slow partial dehydration, specimens were placed in a temperature-regulated aluminum chamber pre-equilibrated and maintained throughout the X-ray exposure at 5 or 10°C by water circulation within the walls of the chamber housing. Specimens were subjected to controlled humidity conditions within the chamber by being suspended (via a mounting screw fixed in the top of the chamber wall) over a cup of saturated salt solution producing a specified RH; a con-

trolled flow of He saturated at the same RH was also passed through the chamber during exposure. After the alignment of specimens with respect to the incident X-ray beam, the chamber was sealed by an air-tight aluminum exit window (the entrance window was made of Mylar), allowing the X-rays to traverse the chamber. Samples were allowed to re-equilibrate for an additional 2 h after placement in the chamber before exposure was initiated.

Equipment Design

A fine-focus Elliott rotating anode X-ray generator type GX6 was used as the source of CuKα X-rays (λ = 1.54 Å, Kα_1 and Kα_2 being unresolved); a nickel filter was used to filter out Kβ radiation. The high voltage generator was set to supply 32 kV to the anode, while the current in the X-ray tube was usually selected at 32 mA. This provided a total flux for the focused, singly reflected beam with Frank's optics (see below) of 5×10^7 photons/s per mm^2, as measured on the position-sensitive X-ray detector (22), assuming an average quantum efficiency of 0.8.

Data were obtained on a vacuum path Franck's-type X-ray camera (23), which contained one curved optical flat allowing the incoming X-ray beam to be reflected up to the critical angle and focused into a vertical line (see specimen geometry below) at the position of detection. The unreflected X-rays and parasitic scatter from the mirror were removed by two pairs of adjustable guard slits, one of which determined the beam height. In our experiments, the beam size at the guard slits was usually 350 μm $\times$ 750 μm (width $\times$ height) when film detection was used and 280 μm $\times$ 1,400 μm when data were collected on the position-sensitive X-ray detector. The entire camera from the mirror assembly to the point of film detection (or alternatively, to the entrance window of the position-sensitive X-ray detector, Fig. 1) was evacuated, hence providing the X-rays with a vacuum path.

Specimen Geometry and Data Detection

Oriented SR membrane multilayers, prepared as described above, were aligned within the specimen chamber (Fig. 1) so that the incoming X-ray beam intersected them at grazing incidence. The beam path was normal to the axis of orientation of the membrane stacks (sedimentation axis), with the beam focused only along the horizontal axis, i.e. the same axis along which lamellar diffraction from the multilayers occurs. In actuality the cylindrically curved glass slides would introduce some curvature to the plane of perfectly oriented membrane stacks, providing sufficient tilt to observe the lamellar diffraction out to an equivalent Bragg spacing of approximately 5 Å.

Samples aligned in this way were exposed between 12 and 18 h at a specimen-film distance of 62.5 mm to obtain the intermediate and high-angle lamellar diffraction pattern with four Ilford-type G X-ray films held in a cylindrical cassette. The same specimen was then exposed 4–6 h with a flat plate cassette placed 250 mm from the specimen in order to resolve the low-angle lamellar diffraction. Alternatively, a linear position-sensitive X-ray detector (LND type 42418, ND Inc., Oceanside, N.Y.: a sealed tube using a Xe-CO$_2$ mixture at 1 atmosphere) was used in place of films to collect the lamellar diffraction data at a specimen-detector anode distance of 330 mm. Details of this instrument will be described in a later manuscript. The data obtained with the detector and Ortec timing electronics (Ortec Inc., Oak Ridge, Tenn.) are displayed as the number of counts vs. channel number on a multichannel analyzer. The spatial resolution of the detector was usually between 150 and 250 μm, with a deviation from positional linearity between 3 and 6%. Preliminary experiments indicate that SR patterns taken on the position-sensitive X-ray detector for times between 20 and 200 s are very similar to those obtained on films (manuscript in preparation). After the exposure, pellets were withdrawn from the chamber and immediately weighed, subsequently dried in an oven at 100°C overnight, dried under vacuum for 3–4 days, and finally reweighed to determine the water content. Most of the diffraction data analyzed in this paper was obtained from films and is discussed below.

Data Reduction

The lamellar diffraction on films was traced with a Joyce, Loebl microdensitometer with a fixed slit height of 0.5 mm, scanning through the center of each arc along the lamellar axis (Joyce, Loebl and Co., Ltd., Gateshead-on-Tyne, England). The relative height of the slit was small with respect to the degree of arcing of the lamellar diffraction (i.e. mosaic spread of the multi-layer), as indicated in Fig. 5. The shape of the background scattering from the SR multilayer specimens was estimated from the shape of the scattering curve obtained from blank slides (24) and the shape of the non-Bragg lamellar scattering from highly ordered lecithin and lipid/protein model membrane multilayer specimens. These latter systems had multilayer periodicities comparable to those of the SR multilayers. The estimated background scattering was sub-tracted from the total lamellar diffraction after scaling the estimated background scattering curve described above to the total lamellar diffraction at both the lower-angle and higher-angle extremes of the total lamellar diffraction function. The background-corrected lamellar dif-fraction obtained by this procedure contained several (five) zero or near zero minima. Such minima are expected, because recent electron microscopic studies on partially dehydrated oriented SR multilayers fixed with OsO_4 vapor under relative humidity and temperature condi-tions similar to those used for the X-ray diffraction experiments clearly show that the unit cell of the multilayer contains the two apposed membranes of the flattened SR vesicle; as a result, the unit cell electron density profile possesses a center of symmetry which requires that the background-corrected lamellar diffraction contain several zero minima over the range of scat-tering angle for which the lamellar diffraction was detected. Hence, we feel that our background scattering subtraction procedure described above is reasonable. The resulting background-corrected lamellar diffraction tracings were digitized in intervals of 1 mm, which corresponds to 0.05 mm on a film placed 62.5 mm from the specimen.

Lamellar diffraction data collected by the position-sensitive X-ray detector with a beam height of 6 mm at the aluminized Mylar entrance window of the detector was transferred from the multichannel analyzer (MCA) memory to a PDP-11 computer memory (Digital Equipment Corp., Maynard, Mass.). The background curve whose typical shape is similar to a mono-tonically decaying exponential function as on films was approximated by short linear line seg-ments and subtracted digitally from the total lamellar diffraction. The active length of the carbon-coated quartz fiber anode was 80 mm, which corresponded to a total of 1,024 channels in the MCA memory. This yields a digitizing interval approximately equal to 0.078 mm on the detector anode for a specimen placed 330 mm from the detector anode. The data was then stored on Dectape (Digital Equipment Corp.) and analyzed by methods similar to those used for films.

Materials

Na-ATP and arsenazo III were purchased from Sigma Chemical Co. (St. Louis, Mo.). Arsenazo III was passed through columns of Chelex 100 obtained from Bio-Rad Laboratories (Richmond, Calif.) to remove Ca^{++} contamination. A23187 and X537A were kindly provided from Dr. Hamill of Eli Lilly and Co. (Indianapolis, Ind.) and from Dr. Burger of Hoffman-La Roche (Natley, N.J.), respectively.

RESULTS

Effects of Centrifugation and Drying on the Ca^{++} Uptake Activity

Fig. 2 shows the results of an experiment where the ATP-dependent Ca^{++} transport by crude SR vesicles in dispersion was monitored by the arsenazo III method. The con-trol experiment in the absence of SR is shown in Fig. 2A, where additions of 10 μM
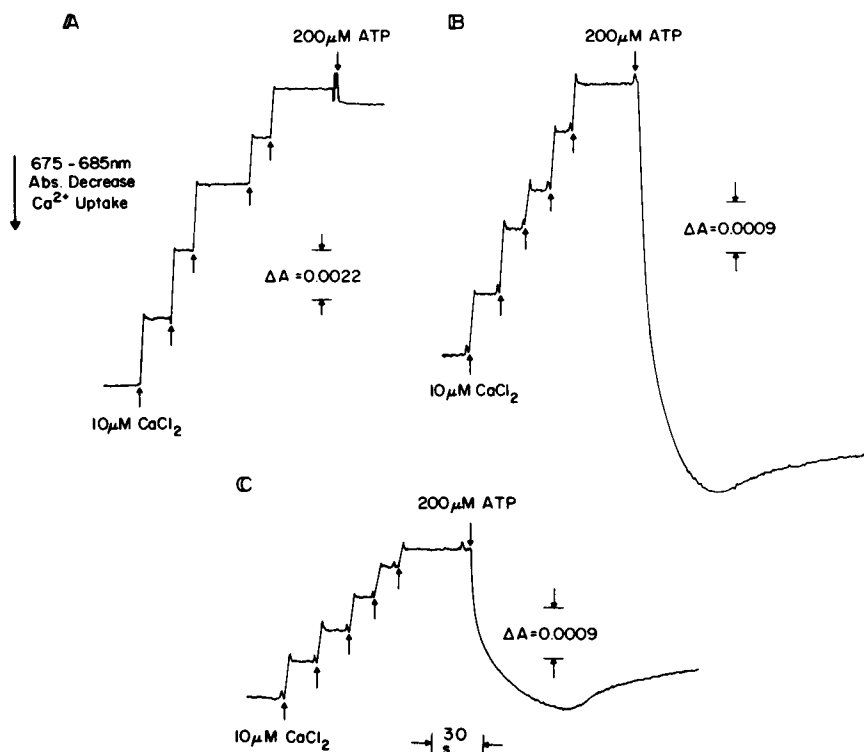
FIGURE 2   A. Changes in light absorbance undergone by arsenazo III upon addition of CaCl₂ and ATP to the reaction mixture in the absence of SR. B. ATP-induced Ca^{++} accumulation by freshly prepared dispersions of SR. C. ATP-induced Ca^{++} accumulation by SR resuspended after centrifugation for 1.5 h at 25,000 rpm and partial dehydration at 90% RH for 15 h at 4°C. The reaction mixtures (2 ml) contained 100 mM KCl, 10 mM MgCl₂, 20 mM Tris maleate (pH 6.8), and 50 μM arsenazo III. In B and C 1 mg SR protein/ml was also present. Additions of 10 μM CaCl₂ and 200 μM ATP are indicated. Steady-state levels of Ca^{++} uptake by SR are given in the text. Temperature was 22°C.

CaCl^2 to a medium containing 100 mM KCl, 10 mM MgCl₂, 20 mM Tris maleate, 50 μm arsenazo III, pH 6.8 (medium II), produces an increase in light absorbance due to formation of the Ca^{++}-arsenazo III complex, which absorbs more light than arsenazo III alone. A negligible decrease in light absorbance is obtained with the addition of 200 μM ATP due to the presence of 10 mM MgCl₂ in the medium, which prevents formation of the Ca^{++}-ATP complex in sizable amounts. In Fig. 2B, the addition of 200 μM ATP to a reaction mixture containing SR results in an abrupt decrease in light absorbance, consistent with Ca^{++} uptake by SR. When the ATP is exhausted (approximately 60 s after the addition), a steady-state accumulation of 154 nmol of Ca^{++} was calculated. The activity of purified SR fraction II (not shown) was measured under identical conditions, and steady-state levels of Ca^{++} accumulations on the order of 100 nmol Ca^{++} were obtained.

Fig. 2 C shows the result of an experiment where the same preparation of SR was

centrifuged for 1.5 h in medium I and was partially dehydrated at 90% RH for 15 h. After this treatment, the multilayers were rehomogenized in medium II in the presence of 50 μM arsenazo III and assayed as above. The average amount of activity after extensive centrifugation and dehydration was usually around 80% of that of the controls. Likewise, SR centrifuged for 3 h and dried 27 h at the same humidity was rehomogenized and assayed with approximately 60% activity. In these experiments, 20 mM Tris maleate was present throughout the procedure to avoid possible pH changes.

Ca^{++} Uptake in Multilayers of SR

The results in Fig. 2 showed that SR multilayers prepared similarly to those used for X-ray diffraction studies maintained most of their functionality when subsequently rehomogenized and assayed as the dispersion. Figs. 3 and 4 show that the SR vesicles conserve their functional activity under conditions identical to those required during X-ray exposure. For these experiments, ATP-dependent Ca^{++} transport was measured in SR multilayers centrifuged in the presence of Ca^{++} and arsenazo III so that known concentrations of both Ca^{++} and arsenzao III were trapped in the extravesicular spaces of the multilayer matrix. In Fig. 3 A, crude SR was sedimented in medium I supplemented with 200 μM arsenazo III and these specimens were maintained in a fully hydrated state. CaCl$_2$ was added to their surface and allowed to reach diffusional equilibration. In control experiments, additions of distilled H$_2$O or 1 M MgCl$_2$ in amounts similar to those used in ATP additions resulted in no significant change of absorbance. The assay was started by adding to the specimen surface 2 μl of 0.1 M ATP, pH 6.8, which produced a decrease in Δ absorbance as a result of ionized Ca^{++} disappearance from the extravesicular space. Similar results were obtained for SR
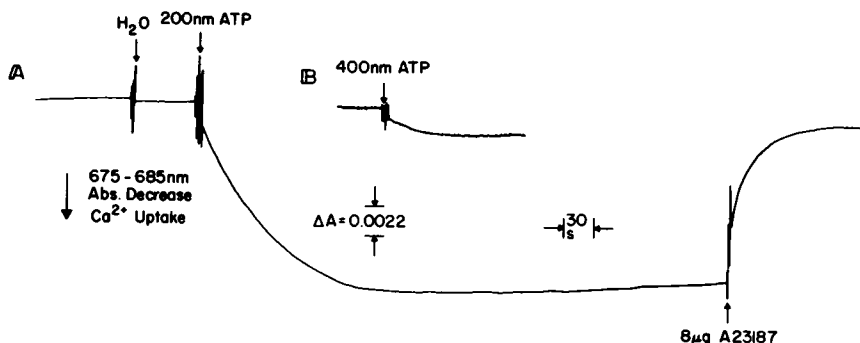

FIGURE 3 A. ATP-induced Ca^{++} accumulation by fully hydrated multilayers of SR after microinjection of 200 nmol ATP onto their surface, followed by Ca^{++} release induced by addition of 8 μg of A23187. B. ATP-induced Ca^{++} accumulation by fully hydrated multilayers of SR after microinjection of 200 nmol ATP onto their surface in the presence of EGTA. Control experiments showing the effect of the addition of 1 μl of distilled H$_2$O are indicated. SR (2.6 mg) was centrifuged at 25,000 rpm for 3 h at 4°C in 100 mM KCl, 2 mM Tris maleate (pH 6.8), and 10 mM MgCl$_2$ (medium I) supplemented with 200 μM arsenazo III and 115 μM Ca^{++} in A, and 200 μM arsenazo III, 10 mM EGTA, and 115 μM Ca^{++} in B.
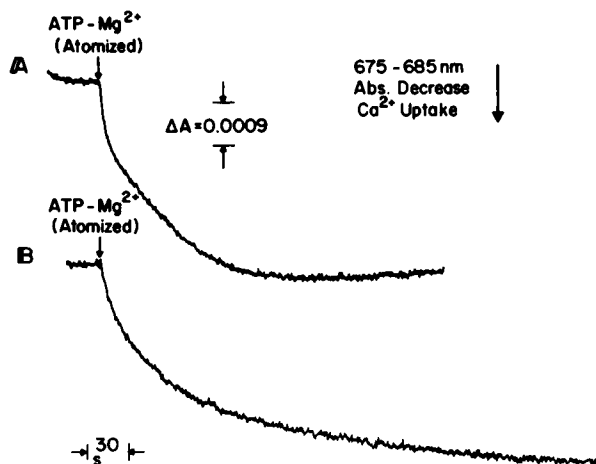
FIGURE 4   ATP-induced Ca^{++} uptake in fully hydrated (A) and partially dehydrated (B) multi-layers of SR after atomization of an ATP-Mg solution (1:2 by mole) above their surface. SR (2 mg) was centrifuged at 25,000 rpm for 3 h in 100 mM KCl, 2 mM Tris maleate (pH 6.8), and 10 mM MgCl$_2$ (medium I), supplemented with 200 μM arsenazo III and 115 μM Ca^{++}, and assayed in the fully hydrated state immediately after centrifugation in A, or partially dehydrated at 90% RH for 23 h at 4°C after centrifugation in B.

multilayers sedimented in the presence of CaCl$_2$ instead of adding Ca^{++} to the SR multilayer surface after centrifugation. The following addition of 8 μg of A23187 produced a rapid increase in Δ absorbance, indicating that the concentration of Ca^{++} in the extravesicular space had increased as a result of Ca^{++} release from SR. The addition of X537A, a second ionophore, which also induced Ca^{++} release from SR vesicles previously loaded with Ca^{++}, produced similar results. Control experiments show that if SR was sedimented in the presence of 10 mM EGTA, the addition of 400 nmol of ATP resulted in minimal changes of absorbance for arsenazo III (Fig. 3B). Analogous results were obtained in SR multilayers prepared in the presence of Ca^{++} when saturating amounts of EGTA were allowed to reach diffusional equilibration within the water spaces of the multilayer matrix. Similar kinetics of ATP-dependent Ca^{++} uptake by SR multilayers (data not shown) were obtained by adding ATP alone, or ATP-Mg (1:1 or 1:2 by mole). These experiments and the effect of the ionophores in releasing Ca^{++} from the SR indicates that Ca^{++} disappearance from the medium is the result of a Ca^{++} uptake by the vesicles rather than the formation of an ATP-Ca^{++} complex.

In Fig. 4 A, multilayers of crude SR were centrifuged in medium I supplemented with 200 μM arsenazo III and 115 μM CaCl$_2$. In these experiments, an ATP-Mg solution was atomized above the surface of these fully hydrated multilayers to minimize the amount of water addition. The Ca^{++} uptake activity was monitored as described above and steady-state levels of Ca^{++} accumulation were obtained in 2.75 min. By comparison, Fig. 4 B shows the results of atomizing ATP-Mg over specimens prepared in a similar manner, followed by partial dehydration for 20–24 h at 90% RH and

4°C, obtaining a steady state in 7.5 min. Although similar steady-state levels of Ca^{++} accumulation were attained by both specimens, the accumulation in the partially de-hydrated specimen was significantly slower. Accurate quantitative measurements of ATP-dependent Ca^{++} transport by these multilayers are difficult to measure because of the change in dye concentration and optical path in the specimens during dehydra-tion. Measurements of the extravesicular space by the $[^{3}H_{2}O-^{14}C]$polydextran method (25) in SR multilayers, which will allow a determination of ion and dye con-centrations within these spaces, are now in progress and will yield a more quantitative assessment of the specific activity of SR multilayers for various degrees of hydration.

Lamellar Diffraction from SR Membrane Multilayers for Three Different Hydration States

Purified SR multilayers were prepared as described above and equilibrated at some RH in the range of 81–95% at 4°C in sealed glass vials with no helium flow. These specimens were then transferred to the X-ray specimen chamber and allowed to re-equilibrate for 2 h before exposure. Upon a preliminary examination of the lamellar diffraction, we found the 86–90% RH range to be optimal. Specimens exposed below 86% RH consistently showed extra reflections whose fundamental Bragg spacing (53 Å) and relative line width and mosaic spread were probable indications of lipid phase separation. The water content of specimens equilibrated below 86% RH was less than 20%. Around 95% RH, there was a significant increase in lattice disorder in the packed vesicle multilayers, evident from the more diffuse higher-angle lamellar data, making it nearly impossible to distinguish the higher-angle maxima from the back-ground scattering. In addition to this, the low-angle lamellar diffraction had a ring-like appearance, which indicates a considerable amount of disorientation in the mem-brane stacks, i.e. an increased mosaic spread. The water content of SR multilayers equilibrated above 90% RH was greater than 30%. Table I summarizes the results of experiments with the SR membranes over the indicated RH range along with the lamellar repeat distance corresponding to that RH. The term resolution is here defined as the quantity ($\lambda/2 \sin \theta_{max}$) where $2\theta_{max}$ is the maximum diffraction angle for which lamellar data was obtained. The average mosaic spread of the lamellar diffraction throughout this RH range was $\pm 30°$ as measured on the films.

In Fig. 5, typical diffraction patterns of purified SR are shown at two specimen-to-film distances for the same relative humidity. A substantial amount of lattice disorder

TABLE I
LAMELLAR REPEAT DISTANCE FOR SAMPLES EQUILIBRATED BETWEEN 86–90% RH

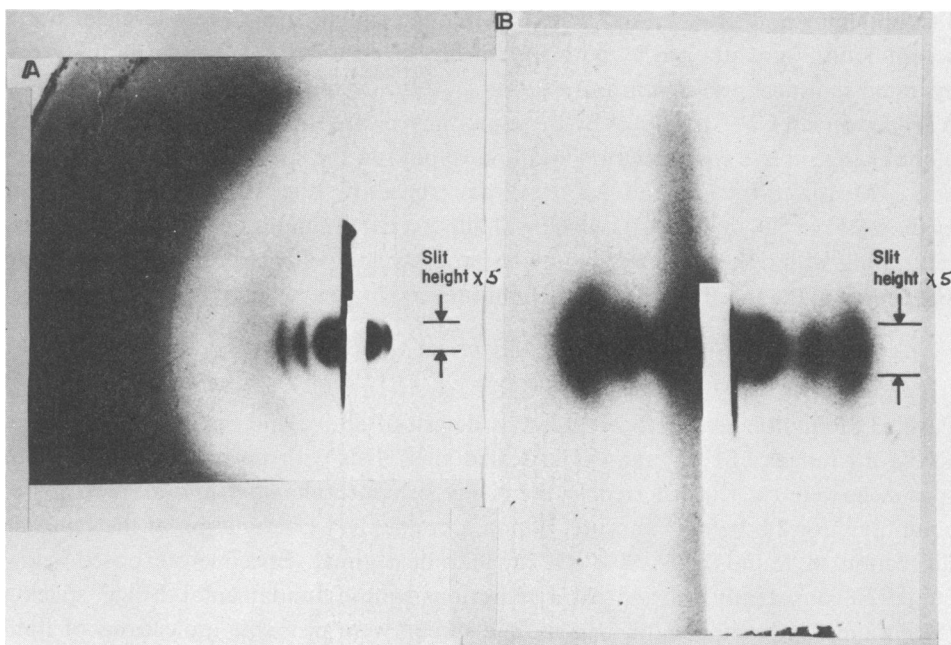| Exp.	RH	Temperature	Lamellar repeat distance	Resolution
	%	°C	Å	Å
1	86	5	153	13
2	87	5	157	12
3	90	10	173	11

FIGURE 5 A. An X-ray diffraction pattern of a partially dehydrated oriented multilayer of purified SR membranes taken at 87% RH. The film was placed 62.5 mm from the specimen in a cylindrical cassette to obtain the higher-angle lamellar diffraction data, i.e. the third, fourth, and fifth maxima. The first, second, and third order lamellar reflections are not resolved. Note the "equatorial" diffraction maximum at $s \sim \frac{1}{10}$ Å, which extends, due to its relatively large mosaic spread, to the lamellar axis. B. Same specimen as in A for a flat film placed 250 mm from the specimen. The lamellar reflections for orders 1, 2, and 3 of a 157 Å repeat are resolved. The second order appears as a shoulder on the third in a microdensitometer tracing and these two reflections constitute the second maximum of the lamellar diffraction data. A fixed slit height of 0.5 mm was set on the microdensitometer at the position of the film and used to obtain the microdensitometer tracings of the lamellar diffraction data. This slit height as shown in the figure has been magnified five times with respect to the lamellar intensity reflections in A and B.

is present, as evident from the monotonically increasing widths for the higher-angle lamellar diffraction maxima (16).

Experimental Intensity Corrections

The corrected lamellar diffraction data $I_c(s)$ of purified SR multilayers as obtained on films is shown for example in Fig. 6 from exp. 2, Table I, after background subtraction and correction by s^2 where s is the reciprocal space coordinate given by $s = 2 \sin \theta / \lambda$. The observed background-corrected lamellar diffraction data is multiplied by one factor of s due to intersection of the reciprocal lattice of the multilayer with the Ewald sphere (Lorentz correction factor) and by another factor of s, a microdensitometry correction arising from the scanning of the arced lamellar diffraction data with a slit of relatively small fixed height. Similar data obtained on the position-sensitive X-ray
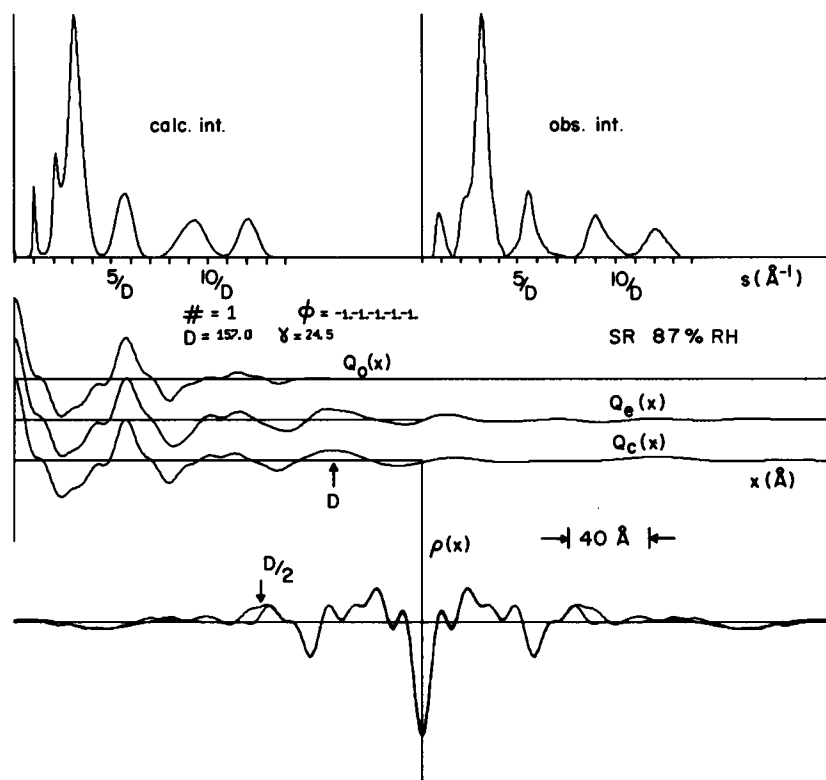
FIGURE 6 High-resolution electron density profile, intensity, and Q-functions calculated by the GFSDM for phase choice one (data from exp. 2). The calculations used all the experimental lamellar intensity function data. The R_Q fit $(0-d/2)$ is given in Table III. The R_I fit over the last three maxima can be found in Table IV. The low-angle maxima of the calculated intensity plot $I_c(s)$ have not been corrected for camera linewidth effects. The description of the Q-functions and $\rho(x)$ plots are the same as that indicated in Fig. 7, only at higher resolution in this case.

detector after background subtraction was corrected by only one factor of s (Lorentz correction factor), since the height of the incident beam and the height of the aluminized Mylar entrance window at the point of detection are both relatively large compared with the arc length of the lamellar diffraction data.

Verification of these corrections to the lamellar diffraction data can be found in a comparison of the Patterson functions $Q_e(x)$ calculated (see following section) from the experimental intensity data $I_e(s)$, obtained on films vs. the linear position-sensitive X-ray detector. The Patterson function calculated from the lamellar diffraction data obtained on films and corrected by s^2 was similar in detail to the Patterson function calculated from the data collected on the position-sensitive X-ray detector and corrected by s. Owing to the internal consistency of these results obtained from different experimental geometries, the corrections applied to the lamellar diffraction data would appear to be valid.

Calculation of the Patterson Function

The Patterson function, designated here as the Q-function for an imperfect finite multi-layer lattice, was calculated from the digitized corrected lamellar diffraction data using the following series approximation as shown by Schwartz et al., Eq. 8 (16):

$$Q(x_j) = 2 \sum_{k=1}^{N_k} I(s_k) \cdot (s_k)^2 \cos(2\pi x_j s_k) \cdot \Delta s. \qquad (1)$$

$$x_j = j\Delta x \qquad\qquad \Delta x = 1\,\text{Å}$$

$$s_k = k\Delta s \qquad\qquad \Delta s = 1/1{,}916\,\text{Å}$$

$$N_k = \text{total number of data points.}$$

The interval Δs is sufficiently small that $I(s)$ is approximately constant within Δs, and therefore the above equation closely approximates $Q(x) = F^{-1}[I(s)]$ where F is the Fourier transform operator. The experimental Q-function, $Q_e(x)$, shown as an example in Fig. 6 from exp. 2, provides a value of the unit cell dimension d from its pseudoperiodicity, equal to 157 Å in this case, necessarily consistent with the sampling interval of the low-angle diffraction maxima in reciprocal space(s).

Analysis of Lamellar Diffraction from Purified SR by the Generalized Fourier Synthesis-Deconvolution Method (GFSDM)

We have applied the GFSDM, as developed by Schwartz et al. (16), to the phasing of the lamellar diffraction from lattice-disordered multilayers of SR. This analysis allows the identification of the autocorrelation function of the unit cell electron density profile and its subsequent deconvolution to provide the unit cell electron density profile. The GFSDM produces a calculated Q-function, $Q_c^{(k)}(x)$ as well as a calculated intensity function $I_c^{(k)}(s)$ for the kth phase combination. Since there are five zeroes in the experimental lamellar diffraction data (where this data approaches the estimated background curve within experimental error), as shown in Fig. 6, these zeroes define six regions of constant phase[1] within the data and there exist in principle 2^5 possible phase combinations. These calculated functions were then compared both qualitatively and quantitatively to their respective experimental $Q_e(x)$ and $I_e(s)$ for all possible phase combinations. Quantitatively, the R_Q value for the Q-function fit has been defined according to the equation as described in step three of the analysis section of Schwartz et al. (16):

---

[1] Inasmuch as the multilayers were formed from a relatively homogeneous population of SR vesicles, we expect and have recently shown by electron microscopy that the unit cell of the multilayer contains the membrane pair corresponding to one flattened vesicle, which would contain a mirror plane in the profile projection between the two membranes of the pair, causing the profile projection to contain a center of symmetry; hence these regions between the zeroes would be of constant phase of 0 or π only.

$$R_Q = \frac{\sum_{i=i_0}^{i_F} [Q_e(x_i) - Q_c(x_i)]^2}{\sum_{i=i_0}^{i_F} [Q_e(x_i)]^2} \qquad (2)$$

A similar equation was used to evaluate R_I, the R-value for the intensity fit. The R_Q fit was calculated for various ranges between $x = 0$ and $x = d$, where d equals the periodicity. However, since the region $d/2 < x \leq d$ is somewhat sensitive to the precise values of γ (the lattice disorder parameter) and d chosen to fit the experimental and calculated Q-function, comparisons of the data were usually based on the R_Q fitting for the range $0 \leq x \leq d/2$. The R_I fit was calculated and used in the analysis only for the high s regions, since a point-by-point difference of the coherent lamellar intensities in this region is unique. This uniqueness is because the high-angle lamellar data is unsampled by the lattice interference function $Z(s)$ and is therefore equal to the unit cell profile structure factor modulus squared $|F(s)|^2$. In addition to this, fitting the coherent intensities over the high s regions avoids the camera line-broadening effects on the first few maxima of the experimental lamellar intensity function. We have noted above that we chose to evaluate R_Q only for $0 \leq x \leq d/2$ and R_I only for the higher-angle regions of $I_e(s)$; this is a result of having considered the multilayer lattice to possess only lattice disorder and neglecting the diffraction camera line-width. This approximation is reasonable because $Q_e(x)$ is predominately $Q_0(x)$ about $x = 0$ only, the maxima in $Q_e(x)$ for $|x| \geq d$ being relatively small in amplitude compared with $Q_e(x = 0)$. While this approximation has no significant effect on the R_Q and R_I values as calculated, and hence the general phasing procedure utilized, it does affect the low-angle region of $I_c(s)$, the region of $Q_c(|x| \geq d)$ and to a greater extent the region of $\rho(|x| \geq d/2)$. More properly, we should calculate $I_c(s)$ according to:

$$I_c(s) = B(s) * [|F(s)|^2 \cdot \{Z(s) * |\Sigma(s)|^2\}], \qquad (3)$$

where $B(s)$ is the diffraction camera line-shape and $\Sigma(s)$ is the Fourier transform of the shape function for a finite lattice containing an average of N unit cells (see Schwartz et al. [16] for details). Hence, $B(s)$ is determined experimentally and γ and N are optimized through a minimization of R_Q for $|x|$ about d, or more precisely through the use of the direct deconvolution method (see Schwartz, et al. [16]). Utilizing this more complete function for $I_c(s)$, the differences between Q_c and Q_e for $|x| \geq d$, between I_c and I_e for small s and between ρ_c and ρ_e for $|x| \geq d/2$ may be virtually eliminated, the latter differences being primarily due to a significantly smaller value of γ required by the I_c-function described by Eq. 3. (These factors affect $\rho_c(x)$ because $\rho_c(x) = \rho_0(x) * \bar{l}'(x)$ where ρ_0 is the unit cell electron density profile and $\bar{l}'(x)$ is the effective average lattice function, the inverse Fourier transform of $B(s) * \{Z(s) * |\Sigma(s)|^2\}$.)

Phase combination	R_Q
1 (– – –)	0.0058
2 (– + –)	0.0068
3 (– – +)	0.0139
4 (– + +)	0.0093

A complete analysis of one set of data (exp. 2) may be summarized as follows. The phasing procedure was initiated by considering the low-resolution electron density profiles to establish the possible phase choice for the first three maxima. From the calculation of the $Q_e(x)$ function using all the intensity data, the periodicity was determined to be 157 Å. The lattice disorder parameter was varied until the almost symmetrical peak at d in $Q_c^{(k)}(x)$ was superimposable on the corresponding peak in $Q_e(x)$, the experimentally determined Q-function. This occurred at $\gamma = 24.5$ Å. The GFSDM calculations for these four possible phase combinations generated from the low-angle intensity data (first three maxima only) were then carried out, and the results are given in Table II.

The R_Q fit was used as the criterion for phasing the low-angle data, since the overall shape of the Q-function will be dominated by the most intense regions (low angle) of the lamellar intensity function; the higher-angle maxima of $I_e(s)$ are sufficiently less intense that one would not expect the variation of their phases to affect this phasing of the low-angle data from considerations of the Fourier sampling theorem. In addition to this, the camera line width will not significantly affect the Q-function for $|x| \leq d$ so that a point-by-point comparison between $Q_c(x)$ and $Q_e(x)$ may be made (16). Therefore, these calculations allow phase combinations 3 and 4 to be eliminated while the quantitative difference between 1 and 2 is probably not significant. In Fig. 7,[2] the low resolution profiles for these two phase choices are shown along with the corresponding $Q_c(x)$ and $Q_e(x)$. Qualitatively, $Q_c^{(k)}(x)$ corresponds well with $Q_e(x)$ for both phase combinations. The calculated electron density profile $\rho_c(x)$ of phase combination 2 is better behaved, however, and tends to flatten out sufficiently near the boundaries of the unit cell at $x = \pm d/2$, whereas 1 does not. However, we chose not to eliminate phase combination 1 at this step of the analysis, and the GFSDM was then applied to the eight possible phase combinations generated from these two phase choices by utilizing the complete set of intensity data. The results of the higher resolution calculations are given in Table III. (We note that the amplitude

---

[2]Owing to the nature of the corrected lamellar intensity data, the calculated and experimental electron density profiles, i.e. $\rho_c(x)$ and $\rho_e(x)$, produced by the GFSDM, appear virtually superimposable, as shown in Figs. 6–9, over the range $-d/2 \leq x \leq d/2$, with minor differences between these functions occurring outside of this range, for reasons described previously. The truncated electron density profile is necessarily superimposable on $\rho_e(x)$. Therefore, no attempt was made to separate these calculated functions so that any small deviations would be more easily recognized in the analysis of the data.
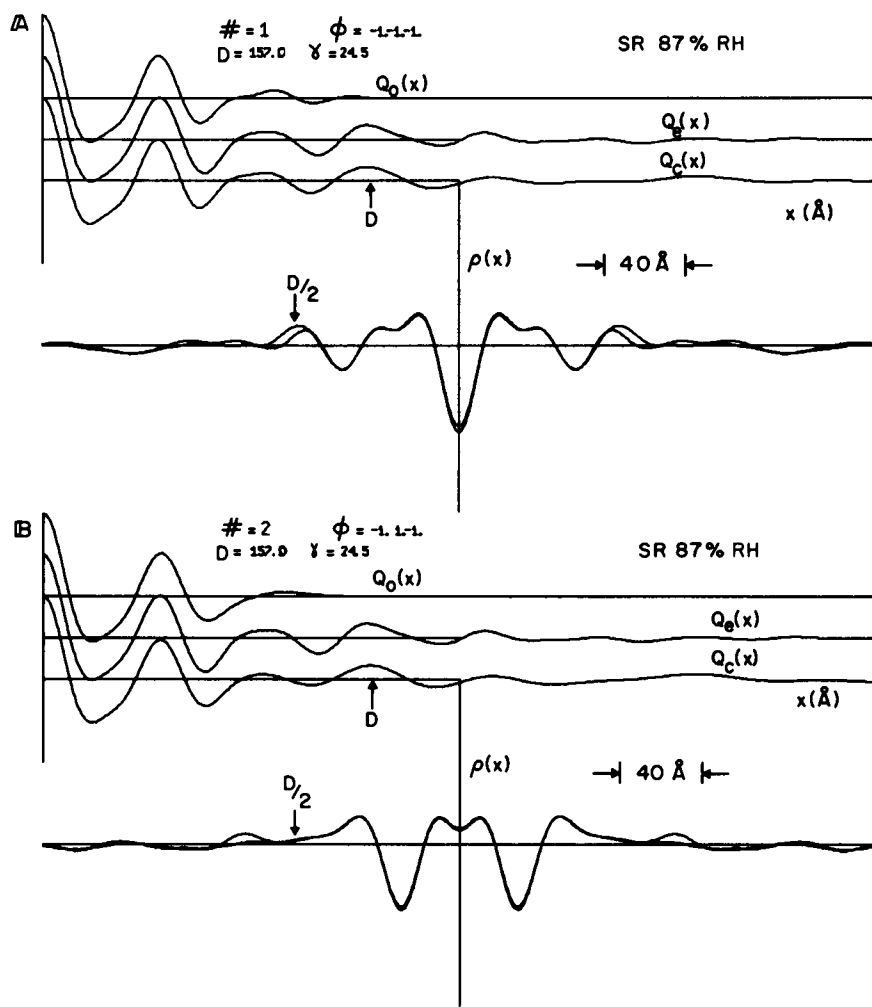
FIGURE 7 Low-resolution electron density profiles and Q functions calculated by the GFSDM for (A) phase choice one and (B) phase choice two. The experimental lamellar intensity function was taken from exp. 2 (γ and d are indicated in the text) and the calculations used the first three maxima only. $Q_0(x)$ is the autocorrelation function of the average unit cell, $Q_e(x)$ is the experimental Q function calculated directly from $I_e(s)$ (the experimental intensity), and $Q_c(x)$ is the calculated Q-function obtained from $I_c(s)$. The R_Q fitting (0–$d/2$) between $Q_e(x)$ and $Q_c(x)$ is given in Table II. The $\rho(x)$ plot represents the superposition of three functions: $\rho_e(x)$, the electron density profile calculated from $I_e(s)$, which is then truncated at $\pm d/2$ to yield $\rho_0(x)$, and $\rho_c(x)$, the electron density profile obtained from $I_c(s)$.

of the third maximum in the experimental intensity function in the region $s \sim (5-6)/d$ is comparable to that of the two higher-angle maxima. The phase of the third maximum, as determined in the GFSDM analysis at low resolution to be -1, could in principle be affected by the phases of the higher-angle maxima, based on consideration of the Fourier sampling theorem. Hence, we also allowed the phase of the third maxi-

Phase combination	R_Q (0–d/2)
1 (− − − − −)	0.0052
2 (− + − − −)	0.0055
5 (− − − + −)	0.0059
6 (− + − + −)	0.0085
9 (− − − − +)	0.0060
10 (− + − − +)	0.0045
13 (− − − + +)	0.0076
14 (− + − + +)	0.0077

mum to vary in the higher-resolution GFSDM calculations; none of the possible phase combinations generated with the phase for the third maximum of +1 possessed R_Q values less than those shown in Table III.)

According to the results of Table III, phase combination 10 had the best Q-function fit over the range indicated. Owing to the statistical accuracy of the data (see further discussion below), it seemed reasonable to also consider the next most probable profile structure in our analysis that arises from phase combination 1 on the basis of this Q-function fit. However, qualitative investigation of the intensity function calculations shown in Fig. 6 indicate that this choice of phasing for the lamellar intensity does not lead to a reasonable calculated intensity function. The distorted shape of the calculated fourth intensity maximum is a clear indication of this. The elimination of phase combination 1 as a probable profile structure is also evident from calculations of the R_I fit defined in Eq. 2 above for the high-angle intensity data (i.e. last three maxima), as shown in Table IV for these three phase combinations. Therefore, we have considered the unit cell electron density profile calculated from phase combination 2 (− + − − −) as the second most probable profile structure generated from the higher-angle data. These two resulting most probable phase combinations 2, − + − − −, and 10, − + − − +, differ only in the phasing of the last lamellar intensity function maximum.

As the data in Table III indicate, the GFSDM calculations yield a hierarchy of most

TABLE IV
HIGH ANGLE R_I VALUES
FOR THE THREE MOST
PROBABLE STRUCTURES

Phase combination	R_I
1 (− − − − −)	0.1000
2 (− + − − −)	0.0550
10 (− + − − +)	0.0599

probable profile structures and therefore the distinction among more probable solutions depends on the statistical accuracy of the data. This is especially true for the case where several phase combinations differing in the phasing of more than one intensity function maximum yield overall R_Q and R_I fits that may not be significantly different. Or alternatively, even when the phases of more intense lower-angle intensity maxima are reliably determined, the phasing of the higher-angle data is often more difficult, due to the greater amount of error in determining these data. This may be the origin of the difficulty seen in the above analysis for the phasing of the last maximum. Therefore, the necessity for independently analyzing additional data sets where both the periodicity and lattice disorder parameter are determined to be different is apparent. The analysis of exp. 3 again indicated that phase combinations 2 and 10 were the most probable profile structures, with phase combination 2 now yielding a significantly smaller R_Q fit for the range $x \leq d/2$, as compared to phase combination 10. (We note that phase combination 1 was not among the four most probable structures in this analysis). This result lends further justification for considering the two most probable structures in the analysis of exp. 2 described above. We therefore conclude that the
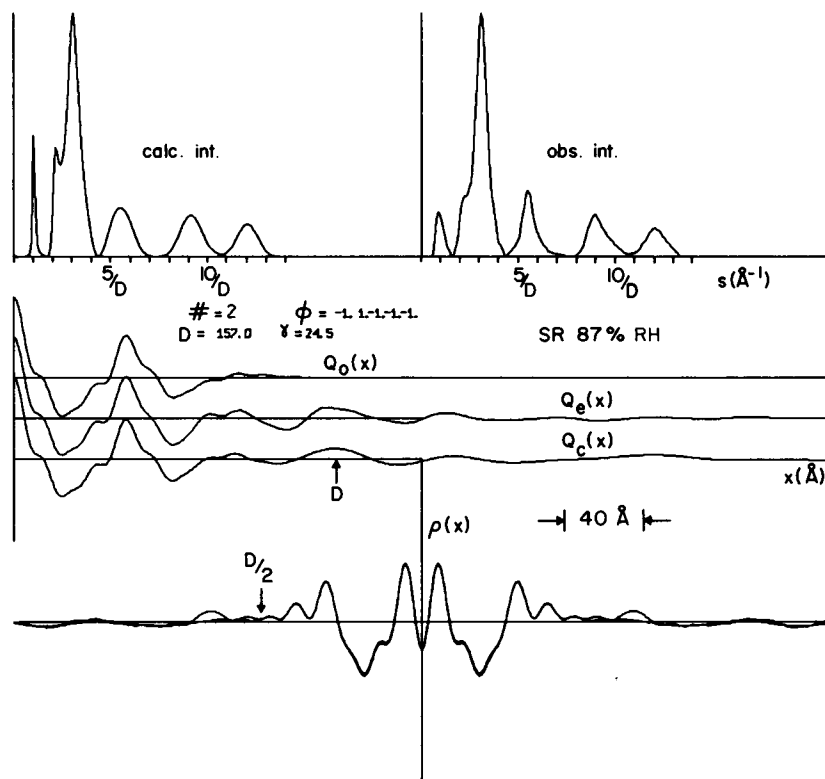

FIGURE 8   High-resolution electron density profile, intensity, and Q-functions calculated by GFSDM for phase choice two. One of two most probable structures for the SR membrane. See Fig. 6 for details.
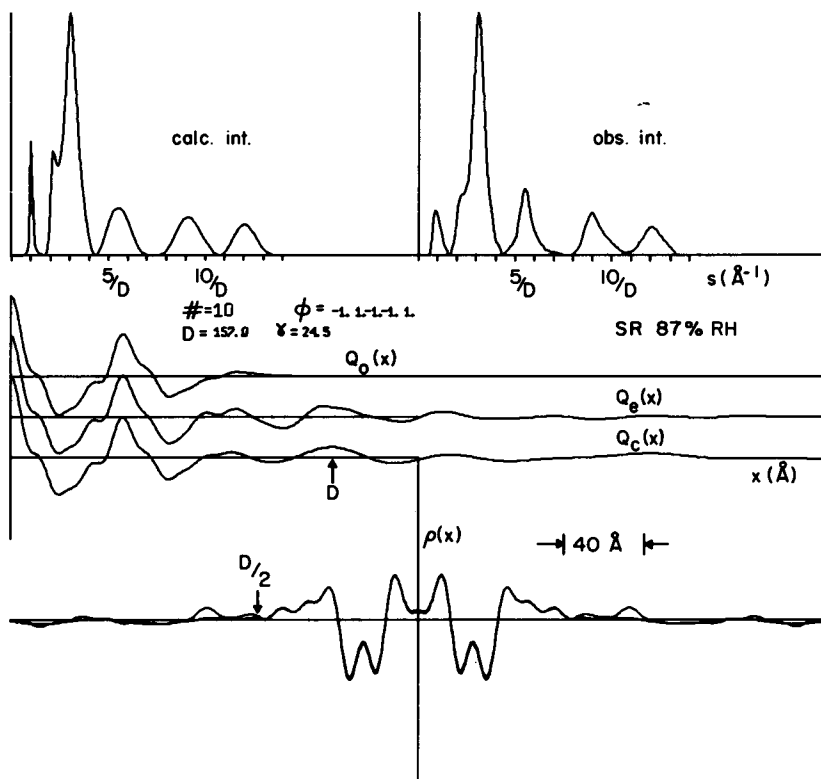
FIGURE 9 High-resolution electron density profile, intensity, and Q-functions calculated by GFSDM for phase choice 10. Alternative structure for the SR membrane. See Fig. 6 for details.

R_Q fitting procedure for two independent data sets equally weights phase combinations 2 and 10.

Close examination of the high-angle experimental lamellar intensity data in Figs. 8 or 9 indicates that between the fourth and fifth maxima, the lamellar intensity does not go to zero experimentally. In Fig. 10, a microdensitometer tracing of this region of $I_e(s)$ clearly indicates this. For the intensity to go to zero in this region, the background curve would need to have a bimodal shape instead of a monotonic, exponentially decaying function. The calculated intensity $I_c(s)$ remains nonzero in this region when the phasing of the last maximum is chosen as that of the next maximum to lower angle, i.e. -1.

In addition to this qualitative comparison, the calculations in Table V verify this quantitatively. Two separate R_I calculations were performed for each of the phase combinations 2 and 10 (data from exp. 2). The first column shows the results of calculating the R_I fit over both the fourth and fifth intensity maxima, while the second column contains the R_I fit over the fifth maximum only. In both cases phase combination 2 yielded the smaller deviation.

These results may indicate that phase combination 2 is indeed the most probable
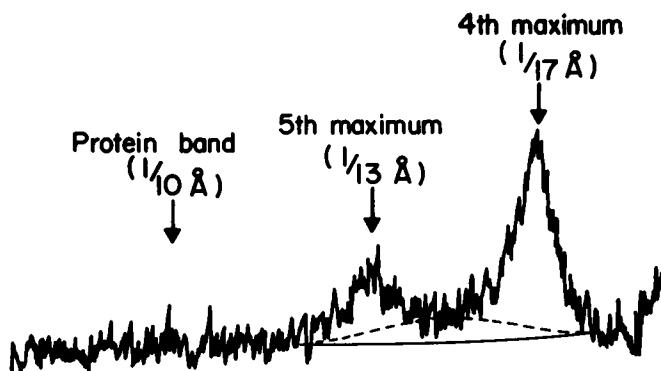
FIGURE 10 Microdensitometer tracing of the higher-angle lamellar diffraction data obtained from partially dehydrated oriented SR multilayers (data from exp. #2, 87% RH). The fourth and fifth maxima of the lamellar diffraction data are indicated, as well as the position of the protein band at $s \sim \frac{1}{10}$ Å, which was very faint on the film from which this tracing was obtained. The solid line represents the estimated background scattering curve, similar to the tail portion of a monotonic exponentially decaying function. The dotted line represents the shape (bimodal) the background curve would have to take on to cause the intensity to go to zero between the fourth and fifth maxima.

choice, since the GFSDM intensity function calculation is more sensitive to the phase choices of less intense maxima than the GFSDM Q-function. This follows from the fact that in $Q_c(x)$ the phase choice for each region of the intensity function exerts its influence uniformly over the region $|x| < d$ in $Q_0(x)$, while in $I_c(s)$ the phase choice of a particular maximum mainly influences the intensity function in that local region of reciprocal space (16). However, even though the above analysis indicates that the unit cell electron density profile corresponding to phase combination 2 is the most probable, the electron density profile generated from phase combination 10 should probably not yet be excluded as a possible profile structure for the SR membrane-pair based on the present data, because even higher-angle lamellar diffraction data unobservable in the experimental noise of these experiments could in principle affect the phase of the highest-angle maximum observed in these data based on considerations of the Fourier sampling theorem.

Finally, we shall briefly discuss the effect of the correction of the total lamellar diffraction for estimated lamellar background scattering, as described in the Data Reduction section, on the GFSDM phasing procedures described above. Although we feel

TABLE V

R_I VALUES FOR HIGH ANGLE DATA FOR
PHASE COMBINATIONS 2 AND 10

Phase combination	R_I (fourth and fifth maxima)	R_I (fifth maximum)
2	0.0245	0.0055
10	0.0271	0.0072

that our background scattering correction procedure as described must be essentially correct, we note that any possible overestimation of background scattering could only occur for $s < 5/d$, thereby causing the minima at $s \sim 1.5/d$ and $s \sim 4.5/d$ in the background-corrected lamellar diffraction to be nonzero. The GFSDM phasing procedure as described above then tends to increasingly favor phase combination 1 in the low-resolution GFSDM analysis (Table II) as the amplitude of these minima increase, as would be expected; however, the hierarchy of most probable phase combinations remained unchanged. We note that phase combination 1 was ultimately rejected on the basis of the higher-resolution GFSDM analysis and that even such unlikely overestimation of background scattering for $s < 5/d$ could not significantly alter the basis for this rejection, i.e. the R_f-value for the higher-angle intensity maxima (Table IV), due to considerations of the Fourier sampling theorem. Therefore, phase combinations 2 and 10 remain the most probable, even allowing for possible but unlikely overestimations of lamellar background scattering for $s < 5/d$.

Substitution Disorder Effects

We have not quantitatively investigated the effects of substitution disorder, which can arise from a variation in the separation of the two membranes within the unit cells in the multilayer. This form of substitution disorder produces an incoherent lamellar scattering underlying the coherent lamellar diffraction, as thoroughly discussed in Schwartz et al. (16). To within experimental accuracy, several minima in the experimental lamellar intensity function obtained from SR multilayers did reach the level of the estimated background scattering, and this is taken as evidence that such substitution disorder effects are in fact minimal. Additional evidence for the absence of a substitution disorder term comes from the almost exact reproduction of $Q_e(x)$ by $Q_c(x)$ in the regions $|x| \leq d$, as calculated by the GFSDM by assuming the existence of only lattice disorder in the multilayer, since the presence of substitution disorder would distort the experimental Q-function in that region (16). This further strengthens the argument presented above, in that the experimental coherent lamellar diffraction does indeed not go to zero between the fourth and fifth maxima, thereby more strongly suggesting that the phase of the last maxima is -1 (i.e. phase combination 2).

Identification of the Intravesicular and Extravesicular Surfaces in the SR Membrane Profile

Hydrated, oriented multilayers of isolated SR membranes have been shown in the preceeding analysis to contain a membrane pair within the unit cell, where the most probable unit cell electron density profile is shown in Fig. 8. Assuming the more physically reasonable situation, that the lattice disorder phenomena observed concern the variations in the separation of vesicles within the multilayer lattice and that the substitution disorder phenomena concern the variations in the separation of the two membranes within a vesicle among the unit cells composing the multilayer, as opposed to the converse situation, the origin at $x = 0$ in Fig. 8 would occur at the center of

the intravesicular space, while the location at $x = \pm d/2$ would occur at the center of the intervesicular space(s) in the SR multilayer lattice. Under this assumption, the identification of these two spaces is unique; this follows because that phase combination which gives rise to the unit cell electron density profile corresponding to the inverted (inside-out) form of the vesicle whose profile is shown in Fig. 8 has a unique $Q_0(x)$ and $|F_0(s)|^2$, which have been shown by the GFSDM to be a less probable profile structure. The assumption concerning the "more physically reasonable situation" is strengthened by the fact that the GFSDM phasing procedure, independently applies to lamellar diffraction data obtained at two different water contents of the multilayers, identified the same unit cell profile as the most probable and indicated that swelling occurred about the location $x = \pm d/2$, i.e. within the extravesicular space, as would be expected.

DISCUSSION

The structure of the SR membrane has been previously investigated by several authors using different isolation and purification procedures for obtaining SR membranes, somewhat different methods for the formation of oriented membrane multilayers, as well as different approaches for analyzing the lamellar diffraction data obtained from oriented multilayers formed from these SR preparations. Worthington and Liu (14) determined an electron density profile of the SR membrane at 17 Å resolution. In their preparations, crude SR was centrifuged for 2–3 days in medium containing sucrose concentrations at over 20% by weight. Using a Patterson function method of structure analysis, they derived an SR membrane profile for multilayers having a lamellar repeat distance ranging from 220 to 270 Å; they suggested that the large asymmetry present in the derived SR membrane profile resulted from the protein molecules residing predominantly on the inside of the vesicle. Dupont et al. (15) prepared multilayers from purified SR in a medium similar to ours with the exception of an addition of 5% glycerol. They obtained a lamellar repeat distance equal to 170 Å for their "dry" samples (25% water). Using swelling methods of structure analysis, they derived an SR membrane profile for these multilayers somewhat different from that of Worthington and Liu (14) and suggested that the protein was located predominantly on the outside of the SR vesicle.

However, neither of the above-mentioned analyses of the lamellar diffraction data from oriented SR multilayers took into account the substantial amount of lattice disorder that we found present even in oriented multilayers formed from purified SR in the absence of sucrose or glycerol. In our preliminary work, we prepared multilayers of crude SR sedimented for 3 hr in more than 20% sucrose (similar to the sucrose content used by Worthington and Liu in their experiments) followed by partial dehydration at 90% RH. Under these conditions, the periodicity of the multilayers was greater than 200 Å; however, these multilayers exhibited a relatively high degree of disorientation in the membrane stacks, as evidenced by the degree of mosaic spread (i.e. extensive arcing) of the lamellar reflections, which Worthington and Liu reduced, presumably through the use of a considerably longer centrifugation. The presence of a consider-

able amount of diffuse lamellar scattering (i.e. incoherent scattering) at lower-angle as well as the broad diffuse lamellar diffraction maxima observed at $s > 6/D$ in reciprocal space indicate that a substantial amount of lattice and probably substitution disorder occurs in such oriented SR multilayers, which must be considered in a proper analysis of such data. Purified SR, sedimented in approximately 10% sucrose before partial dehydration at 90% RH, gave oriented multilayers also, with periodicities on the order of 200 Å, which exhibited much less mosaic spread and lattice disorder in their lamellar diffraction. Therefore, further analysis in our laboratory was then carried out, dialyzing the sucrose from purified SR preparations before preparing samples for X-ray studies in order to obtain optimal orientation in the multilayers without extensive centrifugation, which we have shown to be detrimental to maintaining Ca^{++}-uptake activity in the SR vesicles (see Results section and Marquardt et al. [26]). The structural results we report here should be more comparable in terms of the specimen preparation to those obtained by Dupont et al., since their preparation of purified SR multilayers yielded a lamellar repeat distance (170 Å) similar to our lamellar repeat of 173 Å for SR multilayers containing about 30% water. Details of our methods of preparation are discussed further below.

Preparation of Oriented SR Multilayers for X-Ray Analysis

The preparation of partially dehydrated multilayers of purified and dialyzed SR essentially involves two major steps which include centrifugation of dialyzed dispersions of SR for short periods of time (1.5–3 hr), followed by slow partial dehydration at a specified relative humidity at 4°C for 15–20 hr. This method was found generally useful in our laboratory for producing optimal orientation of hydrated multilayers, not only for the isolated SR and reconstituted SR membrane systems, but also for model membrane systems containing incorporated photosynthetic reaction centers (Pachence and Blasie, in preparation), isolated retinal rod outer segment disk membranes (24, 27),[3] and membranous cytochrome oxidase preparations (28).

Orientation of the multilayers was found to be mostly dependent on the slow partial dehydration step. Multilayers obtained after prolonged centrifugation at comparable states of partial dehydration did not show significantly improved membrane multilayer orientation, as detected by the mosaic spread of their lamellar diffraction. Conversely, variation of the rate and degree of partial dehydration indicated that the slow removal of about 40% of the water (by weight) from fully hydrated multilayer samples appeared to be the major factor in orienting the SR membranes. However, oriented multilayers with a final total water content less than 20% by weight exhibited lipid phase separation phenomena (see Results section). In addition, the SR vesicles used in the present study were purified under zonal rate centrifugation, which makes possible the selection of populations of vesicles relatively homogeneous in their density distribution (i.e. size). This possibly results in an improvement in the packing of vesicles, producing more uniform stacks of membranes within the multilayers.

Ca++ Transport of SR Membranes Suitable for X-Ray Analysis

The structural studies of Worthington and Liu (14) were not supplemented with any data regarding the functional activity of their SR either before or after oriented multilayer formation and X-ray exposure. Dupont et al. (15) measured the ATPase and Ca^{++} uptake activity of their multilayer samples after X-ray exposure in resuspensions of the multilayers. For samples whose lamellar repeat distance was determined to be 190 Å (greater than 30% water), the resuspended SR vesicles showed 80% specific activity for the Ca^{++}-stimulated ATPase and only 30% Ca^{++} uptake activity after X-ray exposure, relative to control SR dispersions. In comparison, our specimens were 80% active, based on ATP-induced coupled Ca^{++} transport after centrifugation and partial dehydration (water content less than 30%). The time scale (on the order of seconds) for collecting data on the position-sensitive X-ray detector is negligible compared to that of centrifugation and partial dehydration (on the order of hours). Since the patterns obtained on films are similar to those taken on the detector, the profile structure of the SR membrane, which we have determined, more closely represents that of the functional membrane more than any obtained previously. Furthermore, we were able to demonstrate the preservation of functionality of the SR membrane, not only after resuspension of SR multilayers, but also directly in partially dehydrated SR multilayers. The activity of multilayers is also evidenced by recent experiments where the ATPase activity has been simultaneously monitored along with Ca^{++} uptake directly in oriented multilayers.

The present data indicate that a substantial Ca^{++} uptake activity is present in partially dehydrated oriented SR multilayers, although precise quantitation of this activity is presently difficult. Experiments are now underway for quantitatively measuring Ca^{++} transport as well as the Ca^{++}/ATP ratio, i.e. the energy efficiency of SR in partially dehydrated oriented multilayers. This data will be obtained simultaneously with lamellar diffraction data collected on the position-sensitive X-ray detector and should make possible a kinetic correlation of structure-function phenomena in the SR membrane.

Structural Analysis on the SR Membrane

By our methods of specimen preparation and data analysis, the unit cell profile for the SR multilayer contains the two apposed membranes of the SR vesicle and was found to have a dimension along the profile axis between 150 and 170 Å for partially dehydrated SR multilayers containing 20–30% water, respectively.

The GFSDM analysis of Schwartz et al. (16), used in this paper, yielded two most probable electron density profiles (generated from phase combinations 2 and 10) for the functional SR membrane that are unperturbed by disorder phenomena in the multilayer. In general, the disorder effects present in SR multilayers are not time-dependent on a scale of seconds, so that the electron density profile calculated by the GFSDM is derived from a statistically stable multilayer lattice and represents the average electron density distribution across the SR membrane on this time-scale. A preliminary interpretation of the SR membrane profile with respect to the molecular composition of the SR membrane will be discussed below.

This particular membrane, LSR, was chosen for study since the interpretation of the electron density profile for the SR membrane is facilitated by the fact that the Ca^{++}-ATPase constitutes 80–90% of the protein in LSR; therefore, a majority of the electron density in the membrane profile that arises from protein is attributable to one particular molecular species. The most obvious feature of the most probable SR membrane profile (the unit cell profile as shown in Fig. 8 contains the two apposed membranes of the SR vesicle; therefore the region from $0 \leq x \leq d/2$ contains one SR membrane profile and the region $-d/2 \leq x \leq 0$ contains its mirror image) is its asymmetry. The following qualitative interpretations of the molecular organization within the SR membrane are based on the most probable membrane profile, generated from phase combination 2 as shown in Fig. 8.

The extravesicular surface of the SR membrane profile ($d/4 \leq x \leq d/2$) contains two relatively electron-dense maxima (whose shapes are resolution limited) whose total profile extension is ~40 Å; this extension is considerably greater than one would expect for a layer of lipid polar headgroups at the surface of a lipid bilayer, even allowing for some delocalization of the headgroups along the profile axis. Therefore, this region at the extravesicular surface of the membrane most likely contains relatively significant amounts of SR protein. The relatively lower electron-dense region of the membrane profile extending form $d/8 \leq x \leq d/4$ has the general feature and dimensions of the hydrocarbon core of a lipid bilayer; the asymmetry of this region of the profile may indicate the penetration of protein from the extravesicular surface of the membrane into this region. The intravesicular surface of the membrane profile ($0 \leq x \leq d/8$) contains a single resolution-limited, relatively electron-dense maximum which could be accounted for simply by a layer of lipid polar headgroups. This preliminary molecular interpretation of the SR membrane profile is strengthened by similar structural studies of SR membranes reconstituted from lipid and Ca^{++}-ATPase.

Electron density profiles have recently been determined for SR membranes reconstituted by the methods of Meissner and Fleischer (29) for various protein-to-lipid ratios, using methods of membrane orientation and diffraction data analysis analogous to those reported here (manuscript in preparation). The appearance of extended electron-dense features arising at the extravesicular surface of the membrane lipid bilayer could be correlated with increasing amounts of protein present in the membrane, accompanied by increasingly significant perturbations occurring within the hydrocarbon core of the membrane lipid bilayer. Further understanding of the details of the molecular organization of the SR membrane are now being sought through such studies and through neutron diffraction studies of both isolated SR membranes and reconstituted SR membranes utilizing deuterated lipid molecules.

NONLAMELLAR COMPONENTS OF THE DIFFRACTION DATA

Diffraction at s ~ $\frac{1}{10}$ *Å associated with protein.* In addition to the recording of the lamellar (meridional) diffraction from oriented SR membrane multilayers, the diffraction along the equatorial direction was noted in two regions. The presence of

the protein in the SR membrane gave rise to a diffraction maximum at $s \sim \frac{1}{10}$ Å whose mosaic spread was much greater than that of the lamellar diffraction. The interpretation of such diffraction has been suggested for other systems (12, 13, 24) and it is thought to arise from interference effects between α-helical polypeptide chain segments with an effective diameter (distance of closest approach) of about 10 Å. In reconstituted SR, this diffraction maximum is more equatorially oriented, which may be correlated with the purer Ca^{++}-ATPase present in these systems as compared to normal SR, and suggests that the α-helical segments have an average orientation normal to the membrane plane. This is substantiated by the presence of a meridional diffraction maximum at $s \sim 1/5.2$ Å in diffraction patterns from the reconstituted SR membrane systems, which arises from the pitch of these so-oriented α-helices.

Diffraction at $s \sim 1/4.6$ Å *associated with lipids.* The broad "equatorial" diffraction maximum $s \sim 1/4.6$ Å arises from the average orientation of the hydrocarbon chain segments in the lipid hydrocarbon core of the membrane. At the temperatures studied, 5 and 10°C, the appearance and position of this broad diffraction maximum, which has a very large mosaic spread compared with the lamellar diffraction, indicates that the lipid chains are in a disordered, melted configuration. There was no indication of a sharp equatorial Bragg reflection at $s = 1/4.2$ Å to indicate a frozen state of the hydrocarbon chains (11), even at the lower temperatures.

Conclusion

The results of these structural studies of the SR membrane, obtained as discussed above, pertain to a highly functional state of the SR membrane which we feel closely approximates that which occurs in vivo.

REFERENCES

1. DUGGAN, P. F., and A. MARTONOSI. 1970. Sarcoplasmic reticulum. IX. The permeability of sarcoplasmic reticulum membranes. *J. Gen. Physiol.* **56**:147.
2. WEBER, A., R. HERZ, and I. REISS. 1963. On the mechanism of the relaxing effects of fragmented sarcoplasmic reticulum. *J. Gen. Physiol.* **46**:679.
3. MARTONOSI, A., and R. FERETOS. 1964. The Uptake of Ca^{2+} by sarcoplasmic reticulum fragments. *J. Biol. Chem.* **239**:648.
4. OHNISHI, T., and S. EBASHI. 1964. The velocity of calcium binding of isolated sarcoplasmic reticulum. *J. Biochem.* **55**:599.
5. MACLENNAN, D. H. 1970. Purification and properties of an adenosine triphosphatase from sarcoplasmic reticulum. *J. Biol. Chem.* **245**:4508.
6. MACLENNAN, D. H., P. SEEMAN, G. H. ISLES, and C. C. YIP. 1971. Membrane formation by adenosine triphosphatase of sarcoplasmic reticulum. *J. Biol. Chem.* **246**:2702.
7. CAMPBELL, K. P., and A. E. SHAMOO. 1977. Depolarization-induced calcium release from light and heavy sarcoplasmic reticulum vesicles. *Biophys. J.* **17**:200a. (Abstr.).

8. INESI, G. 1972. Active transport of calcium ion in sarcoplasmic membranes. *Annu. Rev. Biophys. Bioeng.* 1:191.

9. MEISSNER, G. 1974. Heterogeneity of sarcoplasmic reticulum (SR) vesicles. *Fed. Proc.* 33:1283.

10. LESSLAUER, W., and J. K. BLASIE. 1971. X-ray holographic interferometry in the determination of planar multilayer structure. Theory and experimental observations. *Acta. Cryst.* A27:456.

11. CAIN, J., G. SANTILLAN, and J. K. BLASIE. 1972. Molecular motion in membranes as indicated by X-ray diffraction. *In* Membrane Research. C.F. Fox, editor. Academic Press, Inc., New York. 3–14.

12. HENDERSON, R. 1975. The structure of the purple membrane from *Halobacterium halobium:* analysis of the X-ray diffraction pattern. *J. Mol. Biol.* 93:123.

13. BLAUROCK, A. E. 1975. Bacteriorhodopsin: a transmembrane pump containing α-helix. *J. Mol. Biol.* 93:139.

14. WORTHINGTON, C. R., and S. C. LIU. 1973. Structure of sarcoplasmic reticulum membranes at low resolution (17 Å). *Arch. Biochem. Biophys.* 157:573.

15. DUPONT, Y., S. C. HARRISON, and W. HASSELBACH. 1973. Molecular organization in the sarcoplasmic reticulum membrane studied by X-ray diffraction. *Nature (Lond).* 244:555.

16. SCHWARTZ, S., J. E. CAIN, E. A. DRATZ, and J. K. BLASIE. 1975. An analysis of lamellar X-ray diffraction from disordered membrane multilayers with application to data from retinal rod outer segments. *Biophys. J.* 15:1201.

17. McFARLAND, B. H., and G. INESI. 1971. Solubilization of sarcoplasmic reticulum with Triton X-100. *Arch. Biochem. Biophys.* 145:456.

18. MEISSNER, G., G. E. CONNER, and S. FLEISCHER. 1973. Isolation of sarcoplasmic reticulum by zonal centrifugation and purification of Ca^{2+}-pump and Ca^{2+}-binding proteins. *Biochim. Biophys. Acta.* 298:246.

19. SCARPA, A. 1977. Metallochromic indicators. *Methods Enzymol.* 44: in press.

20. BLASIE, J. K, and C. R. WORTHINGTON. 1969. Molecular localization of frog retinal receptor photopigment by electron microscopy and low-angle X-ray diffraction. *J. Mol. Biol.* 39:407.

21. SCARPA, A., J. BALDASSARE, and G. INESI. 1972. The effect of calcium ionophores on fragmented sarcoplasmic reticulum. *J. Gen. Physiol.* 60:735.

22. GABRIEL, A., and Y. DUPONT. 1972. A position sensitive proportional detector for X-ray crystallography. *Rev. Sci. Instrum.* 43:1600.

23. ELLIOTT, G. F., and C. R. WORTHINGTON. 1963. A small-angle optically focusing X-ray diffraction camera in biological research. Part I. *J. Ultrastruct. Res.* 9:166.

24. SANTILLAN, G. G. 1976. An X-ray diffraction study of isolated retinal photoreceptor disk membranes: The structure of water-washed disk membranes in the dark-adapted and bleached states at 8 Å resolution. Ph.D. thesis, University of Pennsylvania, Philadelphia, Pa.

25. JOHNSON, R. G., and A. SCARPA. 1976. Ion permeability of isolated chromaffin granules. *J. Gen. Physiol.* 68:601.

26. MARQUARDT, J., A. SCARPA, and J. K. BLASIE. 1975. A direct analysis of lamellar X-ray diffraction from disordered multilayers of fully-functional sarcoplasmic reticulum membranes at 10 Å resolution. *Biophys. J.* 15:110a (Abstr.).

27. SANTILLAN, G. G., and J. K. BLASIE. 1975. A direct analysis of lamellar X-ray diffraction from lattice disordered retinal receptor disk membrane multilayers at 8 Å resolution. *Biophys. J.* 15:109a. (Abstr.).

28. BLASIE, J. K., M. ERECINSKA, J. S. LEIGH, and S. SAMUELS. 1977. The structure of a cytochrome oxidase/lipid model membrane. *Biophys. J.* 17:63a. (Abstr.).

29. MEISSNER, G., and S. FLEISCHER. 1974. Dissociation and reconstitution of functional sarcoplasmic reticulum vesicles. *J. Biol. Chem.* 249:302.